Colloids and Surfaces A: Physicochemical and Engineering Aspects 616 (2021) 126230

Contents lists available at ScienceDirect

Colloids and Surfaces A: Physicochemical and Engineering Aspects

journal homepage: www.elsevier.com/locate/colsurfa

Polyethersulfone membranes modified with CZTS nanoparticles for protein and dye separation: Improvement of antifouling and self-cleaning performance

Kasim Ocakoglu [a,*], Nadir Dizge [b,*], Suleyman Gokhan Colak [c], Yasin Ozay [b], Zeynep Bilici [b], M. Serkan Yalcin [d], Sadin Ozdemir [e], H. Cengiz Yatmaz [f]

[a] Tarsus University, Department of Engineering Fundamental Sciences, Faculty of Engineering, 33400, Tarsus, Turkey
[b] Mersin University, Department of Environmental Engineering, 33343, Mersin, Turkey
[c] Mersin University, Advanced Technology Research & Application Center, 33343, Mersin, Turkey
[d] Mersin University, Department of Chemistry and Chemical Processing Technologies, Technical Science Vocational School, 33343, Mersin, Turkey
[e] Mersin University, Food Processing Programme, Technical Science Vocational School, 33343, Mersin, Turkey
[f] Gebze Technical University, Department of Environmental Engineering, 41400, Kocaeli, Turkey

GRAPHICAL ABSTRACT

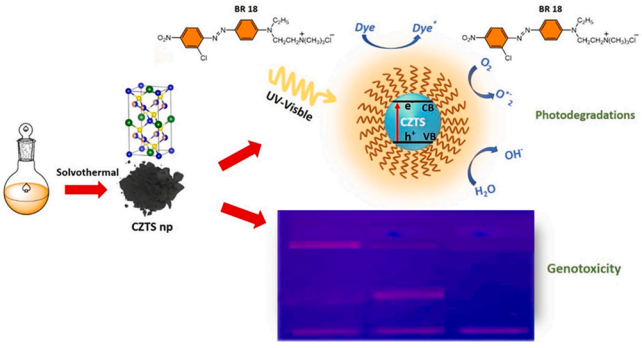

ARTICLE INFO

Keywords:
CZTS nanoparticles
Nanocomposite membrane
Protein separation
Antioxidant
Antimicrobial
Biofilm inhibition
DNA cleavage

ABSTRACT

In this study, a novel polyethersulphone (PES) nanocomposite membrane incorporated with copper zinc tin sulfide (Cu_2ZnSnS_4) nanoparticles (CZTS NPs) was prepared through the phase inversion method. First, the samples containing different copper and zinc ratios in CZTS stoichiometry were prepared and characterized. The effect of copper and zinc ratio changes were examined on the photocatalytic properties of both NPs and nanocomposite membranes. The photocatalytic effect was tested and BR18 dye was degraded at 88.0% efficiency when exposed to visible light for 180 min in the presence of CZTS1.0 NPs catalyst. The results also exhibited that CZTS NPs blended membrane showed good self-cleaning performance. Second, we investigated the antioxidant, DNA cleavage, and biofilm inhibition activities of CZTS NPs. The antimicrobial activities of CZTS NPs were tested against seven microbial strains. The highest 2,2-diphenyl-1-picrylhydrazyl (DPPH) scavenging and chelating activities were found as 81.80 ± 1.75% and 72.19 ± 4.63%, respectively. CZTS NPs exhibited double-strand DNA

* Corresponding authors.
E-mail addresses: kasim.ocakoglu@tarsus.edu.tr (K. Ocakoglu), ndizge@mersin.edu.tr (N. Dizge).

https://doi.org/10.1016/j.colsurfa.2021.126230
Received 29 November 2020; Received in revised form 2 January 2021; Accepted 22 January 2021
Available online 1 February 2021

cleavage activity at 500 mg/L. They showed significant biofilm inhibition as 92.15 ± 5.67% against *Staphylococcus aureus*. CZTS NPs displayed moderate antimicrobial effects against tested microorganisms. Third, CZTS NPs were blended in polyethersulphone (PES) membrane and the morphology as well as performance of the fabricated nanocomposite membranes were systematically investigated by SEM-EDX, porosity, water contact angle, antifouling, and rejection measurements. The water flux of resulting nanocomposite membranes was markedly enhanced due to the introducing of CZTS NPs. Meanwhile, the nanocomposite membranes demonstrated remarkable antifouling properties (flux recovery ratio ~94%) in contrast with the bare PES (flux recovery ratio ~51%) when BSA was filtrated. The high retention of BSA (100%) as well as high permeation flux (73.8 ± 9.8 L/m^2/h) of the CZTS2.00 wt% membrane demonstrated that the constructed nanocomposite membrane possessed the characteristics of a promising membrane for purification of proteins.

1. Introduction

It is well known that the rapid development in the industrial sector improves the standard of human living, but it is also known to play a major role in air, soil, and water pollution. Excessive water use and industrial growth increase the water demand, but a large amount of wastewater is produced [1]. Generally, physical, chemical, and biological treatments are widely used for purification and treatment of water and wastewater [2]. Nowadays, membrane processes are also used intensely to obtaine high-quality water for domestic and industrial demands, treatment and reuse of wastewater, and removal of toxic or recovery of valuable components from various industrial effluents [3,4]. The pressure-driven membrane process for separation of contaminations has attracted great attention in various industrial activities such as chemical, pharmaceutical, textile, water softening, etc. [5,6].

Nanotechnology has great potential to be used in water and wastewater treatment processes to increase treatment efficiency and water supply [7]. The specifications of the materials change as the size of the material reach the nanoscale. Generally, the best performance of the nanomaterials is achieved when their size is less than a certain critical value, which depends on the material [8]. Nanoparticles are one of the new scientific research fields of nanotechnology, due to a wide variety of potential applications in biomedical, optical, chemical, environmental, electronic fields and etc [9]. Moreover, various inorganic nanoparticles (NPs) are of particular interest due to their numerous applications in the fields of catalysis, biomolecular detection, and diagnosis, microelectronics, therapeutic, and attract more attention of researchers [10]. Also, studies reported in the literature have shown that the medical use of NPs includes antibacterial, antifungal, antioxidant agents, anti-inflammatory, anti-diabetic, as well as cancer treatment and diagnosis [11–13]. Recently, the fabrication and application of the biomimetic micro/nano structures including patterns, fibers, porous scaffolds, and microspheres are among the interesting topics like NPs. The biomimetic dynamical micro/nano structures via shape-memory effect have a critical effect on cell behaviors, which have potential applications in drug delivery, cell delivery, bone repair, vascular scaffolding, vascular embolization, skeletal muscle repair, etc [14].

The studies have been focused on selecting an appropriate polymer and adding some effective nanoparticles into the structure of the membrane to improve the characteristics of polymeric membranes [15]. Polyethersulphone (PES) is known as one of the most usable polymers in both laboratory and industrial activities for the fabrication of polymeric membranes due to its high thermal stability, good mechanical characteristics, and excellent heat-aging resistance [16]. However, the hydrophobic property of PES limits its antifouling properties and water flux permeability. To overcome this problem many nanomaterials such as TiO_2[17], boehmite [18], Al_2O_3[19], SiO_2[20], etc. have been strongly studied as necessary additives to improve the performance and structural properties of membranes. Recently, quaternary CZTS which is a P-type semiconducting material is among the prominent nanoparticles due to their direct band gap of 1.4–1.5 eV and high absorption coefficient (10^4 cm^{-1}) in the visible range properties [21]. The need to avoid toxic (such as Cd) or critical (such as In) elements and to increase the sustainability of the photocatalytic heterostructure has increased interest in Cu_2ZnSnS_4 (CZTS).

In this study, the effect of changing precursor metal ratios (Cu/(Zn + Sn)) was investigated for CZTS synthesis. CZTS nanostructures were synthesized according to the given proportions, Cu/(Zn + Sn) = 1.0 (CZTS1.0), Cu/(Zn + Sn) = 0.9 (CZTS0.9) and Cu/(Zn + Sn) = 0.8 (CZTS0.8), as Zn-rich and -poor configurations, and at this stage, the Zn/Sn ratio was kept constant at 1.2. The photocatalytic activities of these nanoparticles were investigated under visible light conditions by using the Basic Red 18 (BR18) dye. Moreover, photocatalytic membrane cleaning was also investigated under UV visible light conditions for 180 min cleaning time. We also investigated the antioxidant, DNA cleavage, and biofilm inhibition activities of CZTS NPs. The antimicrobial activities of CZTS NPs were tested against seven microbial strains. However, the fabrication of a new mixed matrix membrane blended with CZTS NPs was carried out and separation ability, as well as antifouling properties of the fabricated membranes, were investigated using bovine serum albumin (BSA) as a model protein. According to the best of our knowledge, no research paper has been published related to CZTS NPs-blended PES membrane.

2. Materials and methods

2.1. Materials

All precursor salts were purchased from commercial sources and used without further purification. Copper (II) chloride, zinc (II) chloride, tin (II) chloride, and thiourea were purchased from Sigma-Aldrich. Polyethersulfone (PES Ultrason E6020 P, Mw: 58,000 g/mol) was purchased from BASF Company (Germany). Dimethyl sulfoxide (DMSO) and bovine serum albumin (BSA, Mw: 66,000 g/mol) were supplied by Merck Company (Germany). Basic Red 18 (BR18) ($C_{19}H_{25}Cl_2N_5O_2$, Mw: 426.34 g/mol) were supplied by Dystar. Deionized water used in all experiments was obtained from the two-stage Millipore Direct-Q3UV purification system.

2.2. Synthesis of CZTS nanoparticles

The CZTS NPs were obtained by the hydrothermal method without using any surfactant. In a typical synthesis, copper (II) chloride, zinc (II) chloride, tin (II) chloride, and thiourea in the stoichiometric ratio of 2:1:1:4 (for CZTS1.0) were dissolved in ethylenediamine. The ratios for samples CZTS0.8 and CZTS0.9 were as 1.95: 0.9: 0.8: 3.8 and 1.9: 0.8: 0.7: 3.8, respectively. Subsequently, the mixture was transferred to a 100 mL stainless-steel reactor and heated at 230 °C for 24 h. The obtained solid black product was washed several times with ethanol and water and then was dried at 70 °C under vacuum [22].

2.3. Characterizations of CZTS nanoparticles

The crystallographic structure of CZTS was performed using X-Ray powder diffractometer (XRD) (Rigaku Smartlab λ = 154,056 Å) with Cu K_α radiation and was measured within the range of (20°–80°) at the scanning speed of 5 deg/min. Perkin Elmer Frontier device was used for Fourier Transform Infrared (FTIR) measurements. Raman spectra were

recorded using the WITech alpha 300R micro-Raman spectrometer using an excitation source of 532 nm laser. The surface morphologies of the nanoparticles were examined by a Field Emission-Scanning Electron Microscopy (FE-SEM, Zeiss Supra 55), and the samples were coated with platinum before the measurements. The surface image of the NPs were taken on a 100 nm scale at 15.00 keV.

2.4. Photocatalytic activity experiments

Experimental studies were performed in a batch Pyrex photo-reactor (column-shaped) with 500 mL capacity. All properties related to the reactor were given elsewhere [23]. Photodegradation experiments were carried out by six UV–vis light sources (TL-D Super 80 18 W/865, typically 400–700 nm, $\lambda_{Vis,\ max}$ =565 nm, Philips), with an average irradiance of G = 40 W/m^2. Total irradiance values were measured in the central position of the sample holder, using a Delta-T Devices, type BF3 pyranometer. The reactor was surrounded by an aluminium-coated tube for uniform reflection. In the pyrex reactor, the temperature of the reaction was kept around 25 ± 1 °C with cooled air. During the reaction (180 min), samples were taken from the reactor at a determined time and centrifuged at 6000 rpm for 5 min. BR18 dye solution (25 mg/L) were prepared using deionized water. Before irradiation, the samples were left 1 h in dark to reach the adsorption/desorption equilibrium. The photodegradation efficiency, η, was calculated based on the initial absorbance of the dye solution (C_i) and the absorbance after 15, 30, 60, 120, and 180 min (C_f), recorded at the maximum absorbance wavelength for BR18 (λ_{max}=484 nm), using a UV–vis-spectrophotometer (T90 + UV/VIS Spectrometer, PG Instruments Ltd.).

The experiments were conducted under no irradiation (in dark) using the same set-up and parameters as in the photocatalytic experiments to evaluate the impact of adsorption to the removal efficiency of the samples corresponding to a contact time equal to those used in the photocatalytic experiments (1 h in dark followed by 15, 30, 60, 120, and 180 min under irradiation). All experiments were performed in duplicate. Dye removal efficiency was calculated by Eq. (1):

$$Dye\ Removal\ Efficiency,\ \eta\ (\%) = \frac{C_i - C_f}{C_i} \times 100 \quad (1)$$

where C_i was the initial dye concentration and C_f was the dye concentration after a certain reaction time t (min).

Membrane surface fouled by BR18 was photocatalytically cleaned using the same reactor. Nanocomposite membrane was exposed to light for 180 min.

2.5. Antifouling experiments of CZTS NPs

2.5.1. DPPH scavenging activity

The CZTS NPs were assessed for *in vitro* antioxidant activity against 2,2-diphenyl-1-picrylhydrazyl (DPPH) radical [24]. The hydrogen atom or electron donation abilities of the CZTS NPs were tested from the bleaching of the violet-colored methyl alcohol solution of DPPH. Briefly, 2 mL of methyl alcohol solution of DPPH was taken to each tube and then 0.5 mL of sample was added into each tube. Test tubes were shaken gently and stand in a dark place at room temperature for 30 min. After this period, the absorbance of each tube was measured at 517 nm by an ultraviolet spectrophotometer. The same procedure was applied to ascorbic acid and Trolox as positive control. The percentage of the DPPH radical scavenging capacity was calculated based on the Eq. (2). The control reaction contains reagent and solvent except for the CZTS NPs.

$$Capacity\ (\%) = \left(\frac{Abs(control) - Abs(sample)}{Abs(control)}\right) \times 100 \quad (2)$$

2.5.2. Chelating activity

The ferrous ion-chelating activity of the CZTS NPs was determined according to the method of by Dinis et al. [25]. For this test, 0.05 mL $FeCl_2.H_2O$ (2 mM) was taken to each tube and then 0.5 mL of CZTS NPs solution was added into each tube. Then, the reaction was started by adding 0.1 mL ferrozine-1,2,4-triazine (5 mM). The total volume was adjusted to 2.5 mL with the solvent used. The mixture was shaken vigorously and incubated for 10 min at room temperature. Then, for the determination Fe^{2+} chelating ability of CZTS NPs, absorbance of the ferrous iron–ferrozine complex was measured at 562 nm against a blank. As a standard, EDTA was used. The activity of CZTS NPs to chelate ferrous ion calculated according to the Eq. (3). The control reaction contains reagent and solvent except for the CZTS NPs.

$$Metal\ Chelating\ Effect\ (\%) = \left(\frac{Abs(control) - Abs(sample)}{Abs(control)}\right) \times 100 \quad (3)$$

2.5.3. DNA cleavage activity

The DNA cleavage studies were performed using pBR322 plasmid DNA in Tris−HCl buffer. pBR322 plasmid DNA (0.1 μg/μL) in 50 mM Tris−HCl buffer was mixed with CZTS NPs solution (250 μg/mL and 500 μg/mL). An incubation period was then started, which would last for 2 h at 37 °C. After that, samples were loaded with loading dye on a 0.9% agarose gel containing EtBr. The agarose gel was electrophoresed for 2 h at 80 V in Tris/Borate/EDTA buffer and bands photographed under UV light.

2.5.4. Antimicrobial activity

The CZTS NPs were tested for their in vitro antibacterial and antifungal activity against seven microorganisms: Gram-negative bacteria (*Pseudomonas aeruginosa* (ATCC 9027), *Legionella pneumophila* subsp. *pneumophila* (ATCC 33,152), *Escherichia coli* (ATCC 10,536)), Gram-positive bacteria (*Bacillus cereus*, *Enterococcus hirae (ATCC* 10,541*)*, *Staphylococcus aureus* (ATCC 6538)), and one fungus (*Candida albicans*). The minimum inhibition concentrations (MICs) of the CZTS NPs were assessed by the standard broth micro-dilution method [26]. Test microorganisms (about 10^8-10^9 CFU/mL) were inoculated in a medium containing different concentrations of CZTS NPs. Culture media in 96 well microplates were incubated at 37 °C and 120 rpm for one day in a shaker. Then the microplates were read at 600 nm using a microplate reader.

2.5.5. Biofilm inhibition activity

Staphylococcus aureus was used as a model organism for biofilm inhibition. Different concentrations of the CZTS NPs solutions (50, 150, 250, and 500 mg/L) and nutrient broth were added to the wells and then *S. aureus* (about 10^8-10^9 CFU/mL) were inoculated. Then, these wells were incubated in an oven for 72 h at 37 °C. After that, the medium was then removed from the plates and the wells were washed 2 times with distilled water. The plates were left to dry at 80 °C for 1 h and then crystal violet was added to each well and held for 1 h. After 1 h, the crystal violet was removed from the wells and each well was rinsed 2 times with distilled water. Then, each well was rinsed using alcohol, and the measurement was applied using a spectrophotometer at 595 nm. Biofilm inhibition was calculated according to the Eq. (4). The wells with no CZTS NPs were used as a control.

Table 1
Composition of the prepared CZTS NPs blended PES membranes.

Membrane	PES (wt.%)	DMSO (wt.%)	CZTS NPs (wt.%)
Bare PES	14	86.00	0.00
0.25 wt% PES/CZTS	14	85.75	0.25
0.50 wt% PES/CZTS	14	85.50	0.50
1.00 wt% PES/CZTS	14	85.00	1.00
2.00 wt% PES/CZTS	14	84.00	2.00

$$Biofilm\ Inhibition\ (\%) = \left(\frac{Abs(control) - Abs(sample)}{Abs(control)}\right) \times 100 \quad (4)$$

2.6. Preparation of CZTS-blended PES membranes

Bare and CZTS NPs blended PES membranes were prepared by phase inversion method where DMSO was used as the polymer-solvent. The PES polymer was dried in an oven at 80 °C for 2 h before membrane preparation. Four different weights of CZTS NPs (0.25, 0.5, 1.0, and 2.0% wt%, related to the PES weight) and DMSO were added to a flask. The composition of the casting solution is given in Table 1. The mixture was ultra-sonicated for 15 min to well disperse CZTS NPsinto the DMSO solvent. After that, 14 wt% of PES were added and dissolved into the solution overnight, under shaking condition using an orbital shaker at room temperature (25 ± 1 °C). The resulted clear homogenous polymer solution was ultra-sonicated for 10 min to remove air bubbles from the solutions. The bubble-free solution was cast onto a clean and smooth glass plate with a 200 μm casting knife at a speed of 100 mm/s. The casting films on the glass plate were immediately immersed into a coagulation bath containing deionized water (non-solvent bath) at room temperature (25 ± 1 °C). The resulted membranes were separated from the glass plate and they were kept in deionized water overnight. The membranes were carefully cut to a suitable size and deionized water (approximately 1 L) was passed from the membranes under 5 bar before use.

2.7. Characterization of the prepared membranes

Scanning electron microscopy (SEM, FEI, Quanta 650 Field Emission SEM) was used to image the surface and cross-sectional morphology of the PES membranes. For the cross-section image, the PES membranes were fractured after dipped in liquid nitrogen. All samples were dried and coated under vacuum with a thin layer of gold by a sputtering system before taking images.

Water contact angle measurement was carried out using a goniometer (One Attension, Biolin scientific instrument) to characterize surface hydrophilicity of the prepared membranes. The contact angle was measured at least five times of repetition from different places for each membrane to minimize the experimental error.

The overall porosity (ε) was calculated by the gravimetric method. The membranes were dried for 24 h in a desiccator and weighed to measure the weight of the membranes in dry conditions (W_d). Then, the dried membranes were cut in a definite size (5 cm × 5 cm) and then immersed in distilled water for 5 min. After that, water on the surface of the membranes was cleaned carefully with a clean cloth and the membranes were weighed (W_w). The overall porosity (ε) of the prepared membranes was determined using Eq. (5), based on the gravimetric method.

$$\varepsilon = \frac{W_w - W_d}{\rho_w \times A \times \ell} \times 100 \quad (5)$$

where, W_w is the weight of the wet membrane (g); W_d is the weight of the dry membrane (g); ρ_w is the density of pure water at room temperature (0.998 g/cm^3); A is the effective area of the membrane (cm^2), and l is the membrane thickness (cm).

Furthermore, the mean pore radius (r_p) on the basis of the pure water flux and porosity data was calculated by the Guerout–Elford–Ferry Eq. (6).

$$r_p = \sqrt{\frac{(2.9 - 1.75\varepsilon)8\eta\ell Q}{\varepsilon \times A \times \Delta P}} \quad (6)$$

where r_p is mean pore radius (nm); η is water viscosity (8.9×10^{-4} Pa s); l is the membrane thickness (m); Q is the volume of the permeate water per unit time (m^3/s); ΔP is the operating pressure (1 MPa).

2.8. Protein and dye rejection experiments of the membranes

A dead-end filtration system (Sterlitech, HP4750 Stirred Cell) with a cell capacity of 300 mL and membrane effective area of 14.6 cm^2 was used to test the performance of the prepared membranes. The membranes were compacted at 5 bar operation pressure for 30 min to obtain a steady-state permeation flux. After compaction of the membranes, pure water flux was measured for 30 min at the operating pressure of 1 bar and 25 ± 1 °C.

The pure water flux, $J_{w,1}$ (L/m^2/h) was calculated using Eq. (7).

$$J = \frac{V}{A \times \Delta t} \quad (7)$$

where, V is the volume of the collected permeated water (L), A is the effective membrane area (m^2), and Δt is the permeation time (h).

The pure water permeability (L_p) was calculated using Eq. (8).

$$L_p = \frac{Q}{A \times \Delta t \times \Delta P} \quad (8)$$

where Q is the quantity of the permeate sample collected over a period of time (Δt, h) (L); A is the effective membrane area for filtration (m^2); ΔP is the transmembrane pressure (bar).

After 30 min filtration of deionized water, cells were filled with the 250 mg/L of BSA solution as a model organic foulant. The BSA solution was prepared in Phosphate Buffer Solution (PBS, 50 mM, pH 7.4 ± 0.1) to prevent denaturation of the protein. BSA or BR18 dye permeation (J_p, L/m^2/h) was measured for 60 min at a steady pressure of 1 bar and room temperature to study the antifouling properties of the prepared membranes. After 60 min, the fouled membranes were carefully rinsed in deionized water. Lastly, pure water flux after rinsing ($J_{w,2}$, L/m^2/h) was measured for 10 min at a steady pressure of 1 bar.

The protein concentration of the feed (C_f) and the permeate (C_p) were measured according to the Lowry method [27]. The BSA was used as a standard and the results expressed in mg equivalent of bovine serum albumin (BSA) per liter. A UV–vis spectrophotometer (GBC-Cintra-20) was used to determine the concentrations of protein at the wavelengths of 660 nm.

The rejection performance tests of 25 mg/L solution of BR18 dyes were also performed under the operating pressure of 1 bar and pH of 6.5 ± 0.1 with 60 min filtration. The concentration of BR18 dyes in the feed and permeate solution was also measured using a spectrophotometer (Hach DR 3800) at λ_{max} of 484 nm, respectively. The rejection of BSA and dye, R (%) were calculated using Eq. (9).

$$R\ (\%) = \left(1 - \frac{C_p}{C_f}\right) \times 100 \quad (9)$$

where C_p and C_f are BSA and BR18 dye concentrations in permeate and feed samples, respectively.

Moreover, to study the fouling phenomena detail, total fouling ratio (R_t), reversible fouling ratio (R_r), and irreversible fouling ratio (R_{ir}) were calculated using Eqs. (10)–(12), respectively.

$$R_t\ (\%) = \left(1 - \frac{J_p}{J_{w,1}}\right) \times 100 \quad (10)$$

$$R_r\ (\%) = \left(\frac{J_{w,2} - J_p}{J_{w,1}}\right) \times 100 \quad (11)$$

$$R_{ir}\ (\%) = \left(\frac{J_{w,1} - J_{w,2}}{J_{w,1}}\right) \times 100 \quad (12)$$

where, R_r presents the reversible fouling caused by the concentration polarization on the surface of the membrane and R_{ir} indicates the irreversible fouling resulted by adsorption/desorption of the BSA or dye molecules on the surface of the membrane [28].

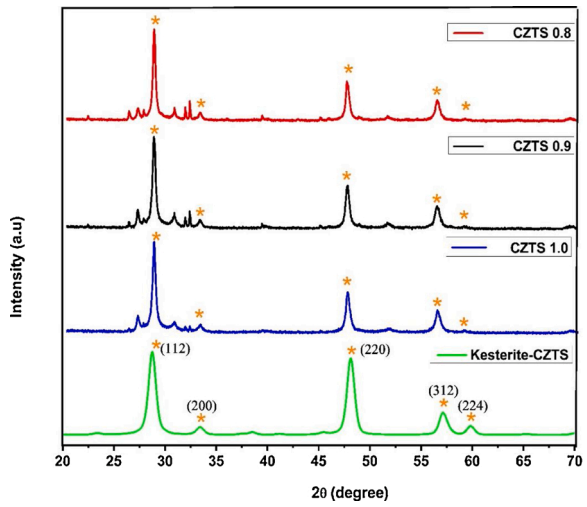

Fig. 1. XRD patterns of the CZTS NPs (CZTS0.8, CZTS0.9, and CZTS1.0).

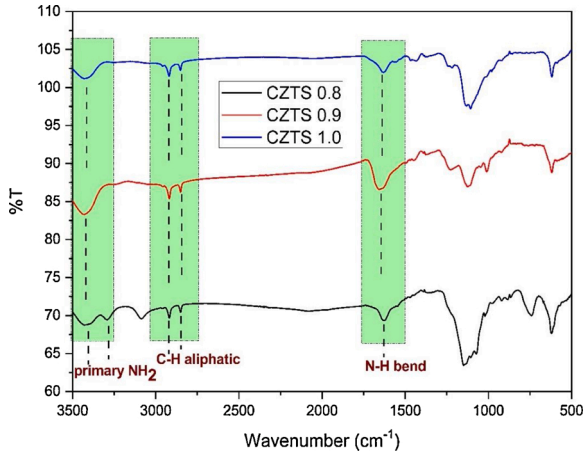

Fig. 2. FTIR spectra of CZTS NPs (CZTS0.8, CZTS0.9, and CZTS1.0).

Flux recovery ratio (FRR) was calculated using Eq. (13) to compare the fouling resistance of the prepared membranes.

$$FRR\ (\%) = \left(\frac{J_{w2}}{J_{w1}}\right) \times 100 \qquad (13)$$

3. Results and discussion

3.1. Characterization of CZTS nanoparticles

3.1.1. XRD characterizations

The stoichiometric ratios of copper chloride, zinc chloride, tin chloride, and sulfur were determined as 2: 1: 1: 4 for an ideal CZTS material. However, Cu/Zn + Sn ratio of CZTS material in pseudo ternary diagram generally varies between 0.8–1.0[29]. Therefore, in this study, CZTS nanoparticles were prepared by changing this ratio in different values such as 0.8−0.9-1.0. The XRD patterns of the CZTS NPs are shown in Fig. 1. According to these patterns, the samples display well-matched kesterite peaks at 2θ = 28.5°, 32.9°, 47.3°, 56.1° and 58.9° corresponding to the (112), (200), (220), (312), (224) lattice planes, revealing a tetragonal phase according to JCPDS card number 26−0575. All the findings were found to match the CZTS nanocrystal thin film related study conducted by the others [30][31]. The other weak diffraction peaks appeared around at 28.5° and 32.9° can be attributed to the planes of the wurtzite structure of CZTS. There is significant similarity in the position of some peaks in the two crystal structures (wurtzite and kesterite) [32]. This is largely due to the change in the proportion of initial metal salts, and as a result, we can conclude that the wurtzite phases are formed, albeit very little [32].

3.1.2. FTIR characterizations

Fourier-transform infrared spectroscopy (FTIR) was used for the detailed structural analysis of CZTS nanopowders. The weak peak around 1630 cm^{-1} shown in Fig. 2 was mainly assigned to NH— vibration. Moreover, broadband containing a double peak in the range 3200–3400 cm^{-1} in the spectrum of CZTS1.0 was observed which was fitted to the primary peaks of NH_2 and OH— groups. However, in the other spectra belonging to CZTS0.8 and CZTS0.9 was only observed a broadband containing a peak in the range 3420 cm^{-1}. Moreover, two weak peaks around 2850−2920 cm^{-1} show the existence of C–H aliphatic groups.

3.1.3. Raman Spectra characterizations

To clarify the composition of the CZTS NPs in more detail, Raman spectroscopy measurements were performed. The micro Raman spectra of the synthesized CZTS NPs were analyzed in ambient conditions using 532 nm laser in the range of 150–500 cm^{-1} as shown in Fig. S1, in which the strongest peak in the range 331–338 cm^{-1} and a minor peak at 287 cm^{-1} were observed. This is consistent with the reported values for the typical kesterite CZTS [31]. Also, the strongest peak at 332 cm^{-1} and a minor peak at 287 cm^{-1} observed in the Raman spectra is compatible with those reported in the literature. In the light of obtained Raman results, it can be said that all materials are generally in the structure of the quaternary kesterite CZTS phase.

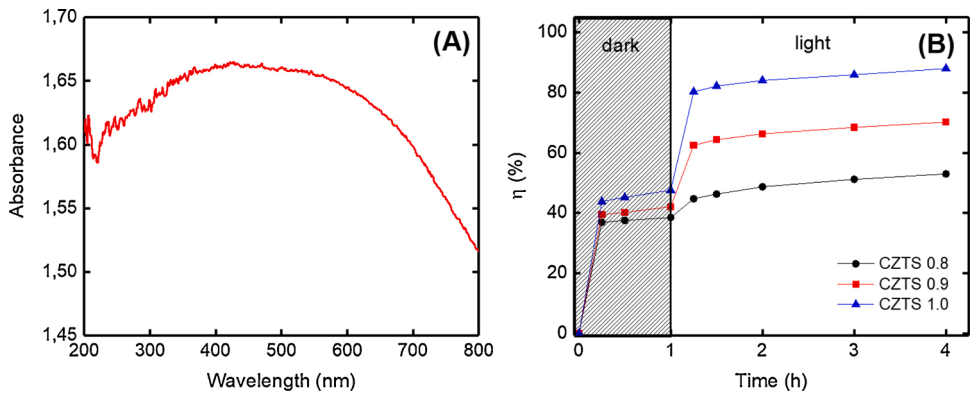

Fig. 3. (A) UV-DRS of CZTS1.0 NPs and **(B)** BR18 dye removal efficiency in dark and under UV–vis conditions for the CZTS0.8, CZTS0.9, and CZTS 1.0.

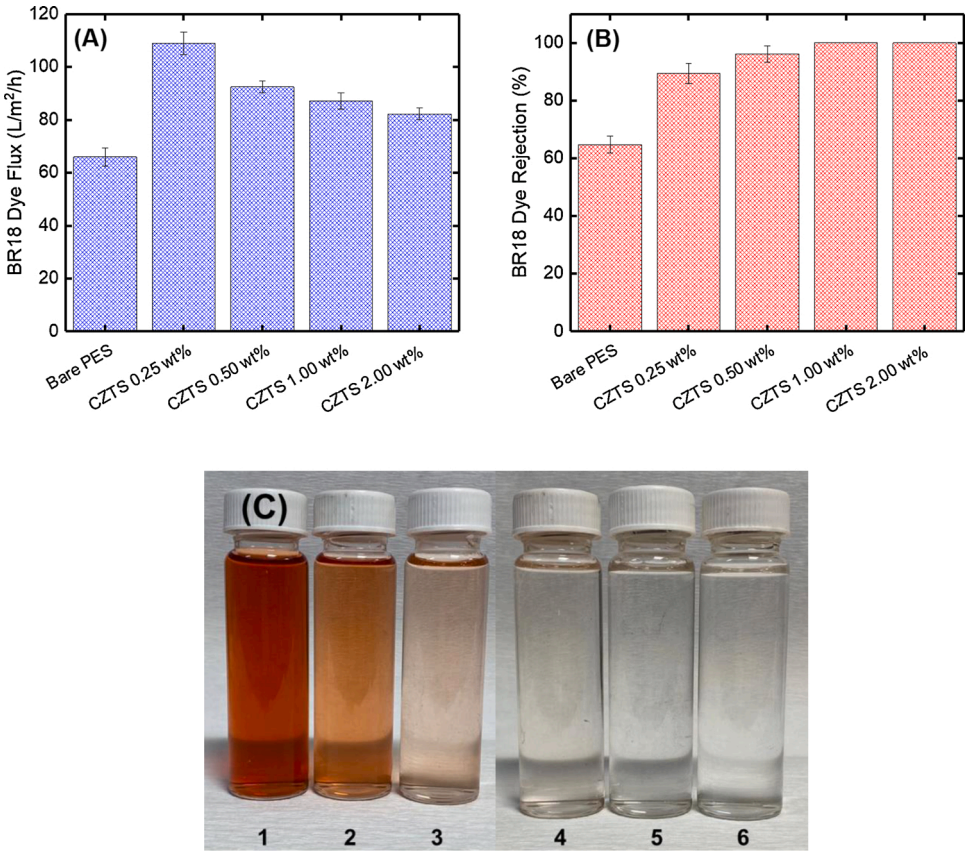

Fig. 4. The filtration of BR18 dye solution. **(A)** flux, **(B)** rejection, **(C)** Photographs of the permeates (1. Inlet BR18, 2. Bare membrane permeate, 3. CZTS0.25 wt% membrane permeate, 4. CZTS0.50 wt% membrane permeate, 5. CZTS1.00 wt% membrane permeate, 6. CZTS2.00 wt% membrane permeate (Experimental conditions: BR18 concentration: 25 mg/L; pressure: 1 bar; filtration time: 60 min).

3.1.4. SEM images

Fig. S2A and S2B show the top view FE-SEM image and particle size distribution histogram of the CZTS1.0 NPs forming in the ethylenediamine solution. Fig. S2A shows a typical FE-SEM image of the samples synthesized with different concentrations of metal precursors. FE-SEM image reveals a large quantity of well-dispersed uniform nanoparticles with the size in the range of 20−30 nm (Fig. S2B). It was observed that the images and particle sizes obtained for the other two samples (CZTS0.8 and CZTS0.9) were mostly the same.

3.2. Photocatalytic experiments

3.2.1. Photocatalytic properties of CZTS nanoparticles

The CZTS1.0 was characterized by UV-DRS (Fig. 3A). The UV-DRS of CZTS has only a broad absorption band around 400–600 nm, proving its absorption only in the visible wavelength region. The effect of Cu/(Zn + Sn) prepared with different ratios between 0.8–1.0 was examined for determination of photocatalytic activity. Cu/(Zn + Sn) = 0.8, 0.9, 1.0, which were named as CZTS 0.8, CZTS 0.9, CZTS 1.0, respectively, was tested by BR18 dye removal efficiency under UV–vis light irradiation. The results demonstrated that CZTS1.0 configuration enhanced better results than CZTS0.8 and CZTS0.9 (Fig. 3B). As the morphology of the three samples are quite similar, this difference in efficiency may be attributed to the better charge transport in the Zn-rich composition of the CZTS nanoparticles. The photocatalytic efficiency was 53.0%, 70.2%, and 88.0% for CZTS 0.8, CZTS 0.9, and CZTS 1.0, respectively for 4 h. The difference in dye removal efficiency might be attributed to different ratios of CZTS NPs. Table S1 shows a summary of recent studies on the photocatalytic degradation of dyes using CZTS NPs.

The photocatalysis phenomenon is based on the redox reactions that take place at the surface of semiconductor materials [33]. The overall photocatalytic process involves three major steps:

i Absorption of light by the semiconductor to generate electron-hole pairs,
ii Charge separation and migration to the surface of the semiconductor and
iii Surface reaction for the water reduction or oxidation reactions.

Photocatalysis reactions can be presented according to the Eq.s (13–18) [34].

$$\text{Semiconductor(photocatalyst)} + h\nu = e_{CB}^{-} + h_{VB}^{+} \quad (13)$$

$$e_{CB}^{-} + h_{VB}^{+} = Energy\ (Heat) \quad (14)$$

$$e_{CB}^{-} + O_2 = O_2^{-}\ (Super\ oxide\ radicals) \quad (15)$$

$$h_{VB}^{+} + H_2O = OH\bullet\ \ (Hydroxyl\ radicals) \quad (16)$$

$$O_2^{-} + Organic\ pollutants = Intermediate = Final\ products\ (CO_2 + H_2O) \quad (17)$$

$$OH\bullet + Organic\ pollutants = Intermediate = Final\ products\ (CO_2 + H_2O) \quad (18)$$

Possible mechanism of degradation of BR18 dye in the presence of CZTS nanoparticles which acts as a catalyst on contact to the Vis light is described in Eq.s (19–24) [31].

$$CZTS + h\nu = CZTS\ (e_{CB}^{-} + h_{VB}^{+}) \quad (19)$$

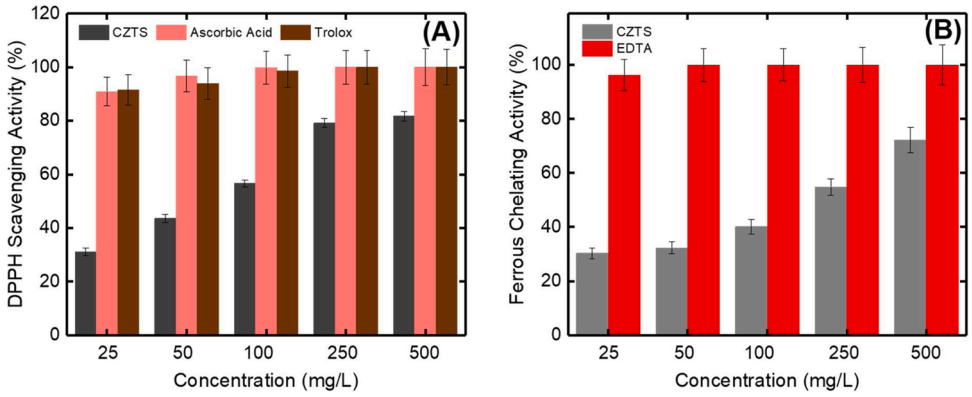

Fig. 5. **(A)** DPPH scavenging activity and **(B)** metal chelating activity.

$$e_{CB}^{-} + O_2 = O_2^{-} \ (Super\ oxide\ radicals) \quad (20)$$

$$h_{VB}^{+} + H_2O = OH\bullet + H^{+} \ (Hydroxyl\ radicals) \quad (21)$$

$$O_2^{-} + H_2O = H_2O_2 \ (Hydrogen\ peroxide) \quad (22)$$

$$H_2O_2 = 2OH\bullet \quad (23)$$

$$OH\bullet + Dye\ molecules = Intermediates = Degraded\ products \quad (24)$$

3.2.2. Dye separation and photocatalytic cleaning properties of CZTS NPs blended membranes

Fig. 4 shows the dye flux and BR18 dye retention performance of the prepared nanocomposite membranes. The steady-state dye fluxes were higher than bare PES membrane (Fig. 4A). However, dye fluxes decreased from 109 ± 4.3–82 ± 2.3 L/m^2/h when CZTS NPs in the membrane increased from 0.25 to 2.0 wt.%. The dye flux of bare membrane was 66 ± 3.5 L/m^2/h. BR18 dye rejection increased from 89.5–100% when CZTS NPs in the membrane increased from 0.25 to 2.00 wt.% (Fig. 4B). The dye rejection was only 64.8 ± 3.0% for bare membrane. The results clearly showed that CZTS NPs blended in the PES membranes improved dye rejection efficiency. The photograps of the permeates are shown in Fig. 4C. A more colorless filtrate was obtained when the CZTS NPs ratio in the membrane was increased. A complete dye removal was obtained for CZTS1.00 wt% and CZTS2.00 wt% membranes. CZTS nanoparticles affected positively the filtration performance of BR18 dye solution. The increase in BR18 dye adsorption with the increase of CZTS NPs dosage in the PES membrane can be attributed to increased adsorbent surface and availability of more adsorption sites throughout membrane surface [35]. In addition, electrostatic attraction exists between the negatively charged surface of the CZTS NPs and positively charged cationic BR18 dye molecules at pH of 6.5 [36].

Photocatalytic cleaning properties of CZTS NPs blended membrane was also investigated. The photographs of bare membranes and CZTS NPs-blended membranes exposed to UV–vis light are shown in Fig. S3. The surfaces of PES/CZTS2.00 wt% membranes before and after photo-cleaning are shown in Fig. S3(A–D). The clean PES/CZTS2.00 wt% membrane was shown in Fig. S3A and it was severely fouled after BR18 dye filtration (Fig. S3B). It can be clearly seen that photo-cleaning removed BR18 dye molecules from the membrane surface after 3 h exposition of UV–vis light. The color of the membrane was dark-reddish after filtration and color turned light pink after 1 h exposition of UV–vis light (Fig. S3C). After 3 h exposition, the color turned from light pink to pale orange (Fig. S3D).

3.3. Antimicrobial properties of CZTS nanoparticles

3.3.1. DPPH scavenging activity

The DPPH method is a well-known rapid and convenient method, which is simply used for the screening of many samples for radical scavenging activity. The results of the investigation of antioxidant screening revealed that CZTS NPs exhibited a well radical scavenging capacity in a dose-dependent manner compared with the standard ascorbic acid and Trolox (Fig. 5A). CZTS NPs displayed a minimum of 31.07 ± 1.34% DPPH scavenging activity at 25 mg/L concentration whereas ascorbic acid and Trolox displayed 90.85 ± 5.34 and 91.64 ± 5.68, respectively. However, when the concentration was increased to 500 mg/L, the NPs exhibited a maximum scavenging activity of 81.80 ± 1.75% while ascorbic acid and Trolox exhibited as 100%. CZTS NPs showed 31.07 ± 1.34%, 43.58 ± 1.48%, 56.60 ± 1.21%, 79.17 ± 1.69%, and 81.80 ± 1.75% scavenging activity at concentrations of 25, 50, 100, 250, and 500 mg/L respectively. It was shown that the radical scavenging activity of CZTS NPs was concentration dependent. Duman et al. synthesized CuO NPs and reported that they exhibited concentration-dependent effective antioxidant activity [37]. Merugu et al. synthesized bimetallic Ag/Cu and Cu/Zn NPs and reported that Ag/Cu and Cu/Zn NPs exhibited 58% and 40% DPPH radical scavenging activity at 100 mg/L [38]. Our findings were demonstrated similar radical scavenging activities with their findings.

3.3.2. Metal chelating activity

Under favorable conditions, reactive oxygen species (ROS) constantly occur as by-products throughout the electron transport system and other metabolic activities at basal levels, and ROS is produced by metal-catalyzed oxidation reactions. The ROS mainly comprise singlet oxygen (^{1}O2), hydroxyl radical (OH$^{\bullet}$), hydrogen peroxide (H_2O_2), and superoxide ($^{\bullet}O_2^{-}$). These are harmful and cause extensive damage to DNA, protein, and lipids and thereby affect normal cellular functioning [39]. However, they are unable to cause damage, as they are being scavenged by different antioxidant mechanisms. Transition metals (especially Fe(II)) play a crucial role as pro-oxidants of the oxidation process, including lipid peroxidation [40]. In addition, oxidative stress occurs when excess oxidative free radicals are produced in cells [41]. In order to determine the antioxidant capacities of the CZTS NPs ferrozine test was applied. Metal chelating activities are presented in Fig. 5B compared to standard (EDTA) material. The metal chelating activities were found as 30.27 ± 1.98%, 32.32 ± 2.16%, 40.13 ± 2.82%, 54.79 ± 3.09%, and 72.19 ± 4.63% for at concentrations of 25, 50, 100, 250, and 500 mg/L respectively. The metal chelating activity of the CZTS NPs was found to be less than EDTA at the same concentration. However, in light of our findings, CZTS NPs can be used as antioxidant agents after further researches.

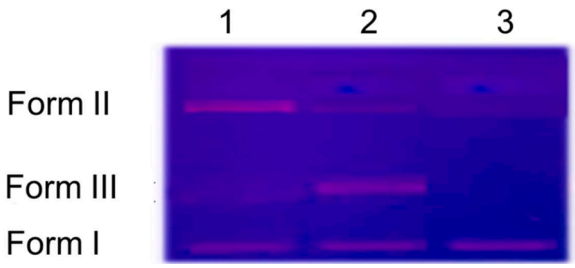

Fig. 6. DNA cleavage activity of CZTS. Lane 1) pBR 322 DNA +250 μg/mL CZTS, Lane 2) pBR 322 DNA +500 μg/mL of CZTS, Lane 3) pBR 322 DNA.

Table 2
The minimum inhibition concentration (MIC) of test microorganisms.

Microorganisms	CZTS
E. coli	512
B. cereus	128
S. aureus	256
E. hirae	256
P. aeruginosa	128
L. pneumophila subsp. *pneumophila*	128
C. albicans	256

3.3.3. DNA cleavage ability

The chemical nuclease activities of the CZTS NPs were evaluated by using pBR322 plasmid DNA in Tris/Borate/EDTA buffer 37 °C. When the plasmid DNA is conducted by agarose gel electrophoresis, the supercoiled circular form (Form I) is observed to migrate relatively faster than the nicked circular form (Form II) and linear form (Form III). Gel electrophoretic separation image of pBR322 DNA treated with the concentration of 250 μg/mL and 500 μg/mL CZTS NPs is presented in Fig. 6. Obtained results showed that CZTS NPs were exhibited chemical nuclease activity, whereas untreated DNA did not exhibit cleavage activity in Lane 3. CZTS NPs showed single strand cleaved DNA activity at 250 μg/mL while they showed double-strand cleaved DNA activity at 500 μg/mL concentration (Lane 1 and Lane 2). Similar to our results, Duman et al. [37] reported that when CuO NPs interacted with plasmid DNA, the supercoiled circular form was broken and the intensity of the nicked circular form increased. Bazrafshan et al. [42] investigated the interaction of ZnO nanorods with DNA molecules and they reported that ZnO nanorods caused DNA damage. The results attribute to DNA cleave demonstrate their ability to inhibits the growth of the pathogenic microorganism by cleaving their genome [43].

3.3.4. Antimicrobial activity

In vitro anti-bacterial and anti-fungal properties of CZTS NPs were investigated against six bacterial and one fungal strains. The MIC values in μg/mL were determined and the results are presented in Table 2. CZTS NPs were exhibited MIC values of 512,128, 256, 256,128,128 and 256 μg/mL against *Escherichia coli*, *Bacillus cereus*, *Staphylococcus aureus, Enterococcus hirae, Pseudomonas aeruginosa, Legionella pneumophila* subsp. p*neumophila, Candida albicans,* respectively. The results of the study showed that CZTS NPs were exhibited moderate activity against tested microorganisms except for *Escherichia coli*. *Escherichia coli*. was found to be the most resistant bacteria to CZTS NPs. Merugu et al. [38] synthesized and characterized Ag/Cu and Cu/Zn NPs and reported that they were inhibited the growth of *Alcaligenes faecalis*, *Klebsiella pneumoniae*, *Citrobacter freundii*, *Staphylococcus aureus* and *Clostridium perfringens*. Carbone et al. [44] indicated that Cu/Zn mixed oxide NPs effectively inhibited *Escherichia coli*. Saedi et al. [45] synthesized sulfur NPs and reported that sulfur NPs were inhibited the growth of *Staphylococcus aureus*, *Aspergillus flavus*, *Listeria monocytogenes* and *Candida albicans*. They also reported that the sulfur NPs did not inhibit the growth of *Escherichia coli* with MIC value of 1024 μg/mL. Our results displayed more effective antimicrobial activities than their findings. The main antimicrobial mechanism of NPs is to destroy the structure of the microorganism cell membrane, release NPs and produce ROS to damage intracellular structures as well as modulate signal transduction pathways of microorganisms. The different results obtained in antimicrobial studies can be attributed to this mechanism and also DNA cleavage abilities of CZTS NPs.

3.3.5. Biofilm inhibition activity

The biofilm-forming activity of *Staphylococcus aureus* is recognized as a major cause of persistent human infections and plays an important role in increasing antibiotic resistance. For this reason, attacking biofilms is an alternative way recommended to combat bacterial infections [46,47]. Thanks to advances in nanotechnology, new antimicrobial agents have been developed in recent years. Nanomaterials have a wider germicidal range than antibiotics and even showed responses against a variety of cell types [48]. For these reasons, the anti-biofilm effect of CZTS NPs at 50, 100, 250, and 500 mg/L concentration against the *Staphylococcus aureus* biofilm formed on polystyrene microplates was tested by screening the population of viable cells. The obtained result is presented in Fig. 7. CZTS NPs provided 60.66 ± 3.45%, 88.29 ± 4.78%, 89.28 ± 5.06%, and 92.15 ± 5.67% reduction in biofilm formation by *Staphylococcus aureus* at concentrations of 50, 150, 250, and 500 mg/L respectively. The inhibition of biofilm formation may be due to ROS production. Miao et al. [49] reported that CuO NPs inhibit biofilm formation by negatively affecting the physiological and ecological aspects of the microorganisms in biofilms. Applerot et al. [50] and Dwivedi et al. [51] reported that ZnO NPs showed important inhibition in biofilm formation. Their studies were also explained that the ROS formation is the major reason for antibiofilm activity. The metal nanoparticles come into contact with bacteria, they induce a significant rise of ROS. This stress leads to killing the bacteria. The results of this study reveal that

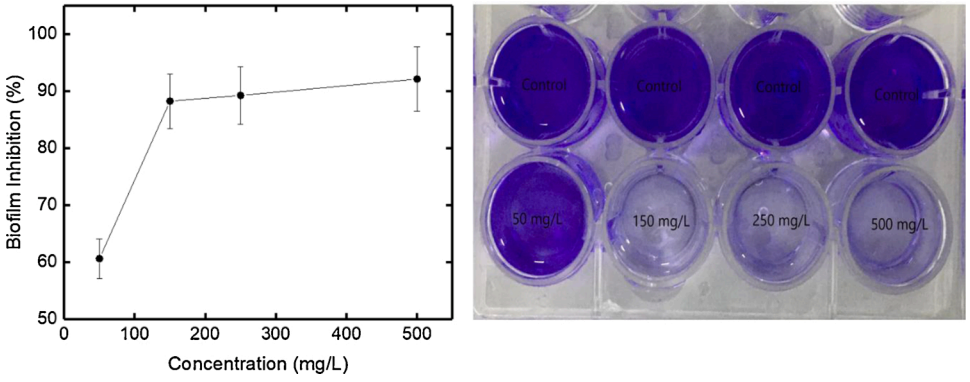

Fig. 7. Biofilm inhibition activity.

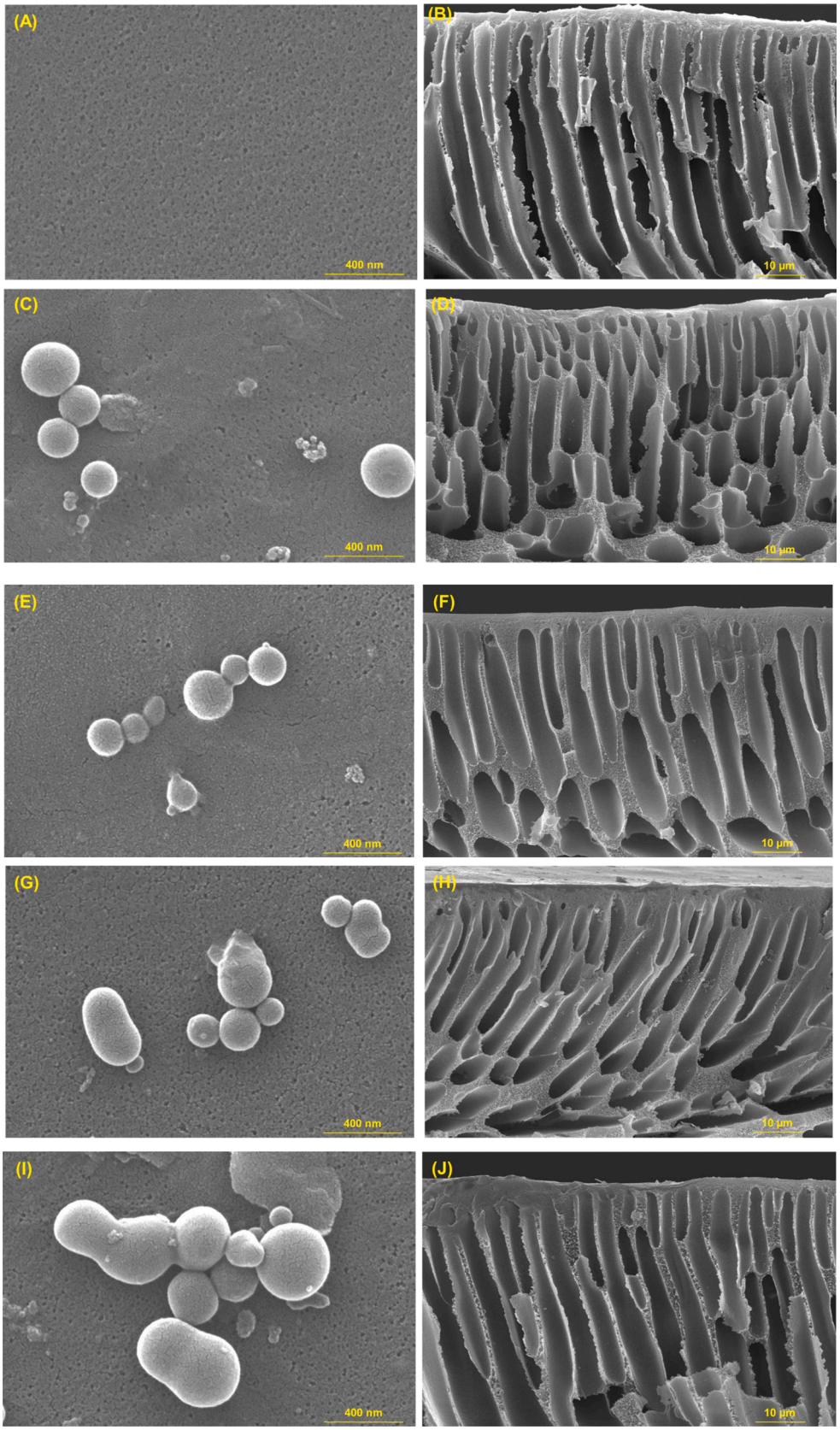

Fig. 8. Surface SEM of nanocomposite membranes in different loading CZTS NPs (**A** and **B**: top surface and cross-section of bare membrane; **C** and **D**: top surface and cross-section of CZTS 0.25 wt%; **E** and **F**: top surface and cross-section of CZTS 0.50 wt%; **G** and **H**: top surface and cross-section of CZTS 1.00 wt%; **I** and *J*: top surface and cross-section of CZTS 2.00 wt%).

Table 3
Porosity, mean pore size, and contact angle of CZTS-blended composite membranes.

Membrane type	Porosity (%)	Mean pore radius (nm)	Contact angle (°)
Bare PES	66.6 ± 1.0	34.6 ± 0.25	73.4 ± 0.4
CZTS 0.25 wt%	65.8 ± 1.8	36.1 ± 0.19	69.2 ± 0.5
CZTS 0.50 wt%	62.4 ± 0.9	37.5 ± 0.14	66.4 ± 0.3
CZTS 1.00 wt%	61.6 ± 1.5	36.5 ± 0.32	66.2 ± 0.3
CZTS 2.00 wt%	58.1 ± 0.6	34.9 ± 0.09	68.9 ± 0.5

CZTS NPs can be investigated as a potential antibiofilm agent after further studies.

3.4. Characterization of CZTS NPs-blended PES membranes

Fig. 8 shows the surface and cross-section SEM micrographs of the prepared membranes. All nanocomposite membranes showed an agglomeration on the surface of membranes. The agglomeration of nanoparticles on the structure of nanocomposite membranes increased with the increasing of CZTS nanoparticle concentration. Cross section structure of nanocomposite membranes remained unchanged and finger-like structure was obtained for all membranes. Fig. S4, which shows the surface EDX spectra of the bare and nanocomposite membranes, proved that the CZTS nanoparticles were within the structure of PES nanocomposite membranes. The EDX spectra of bare PES membrane showed the elementary components was composed of C, O, and S. In addition to C, O, S elements found in bare membrane, the EDX elemental spectra of all the nanocomposite membranes further confirmed the presence of Cu, Zn, and Sn, which proved CZTS NPs was within the membrane structure. Regarding these captured micrographs, no structural flaw (defects and brittleness) was observed on the surface of the prepared nanocomposite membranes.

The overall porosity, mean pore size and contact angle of the prepared membranes are presented in Table 3. The porosity and contact angle of the nanocomposite membranes decreased after blended of CZTS NPs. However, mean pore radius increased compared to bare membrane.

3.5. Membrane performance

3.5.1. Pure water flux

The dead-end technique was used to investigate the flux and rejection performance of prepared nanocomposite membranes, and the obtained results were illustrated in Fig. 9. As can be seen from Fig. 9A, the pure water flux of all nanocomposite membranes increased from the bare PES to PES/CZTS 1.0 wt%. Such flux enhancements could be described by both the desired distribution of CZTS NPs in the matrix of membrane and enhancement of the hydrophilicity and mean pore size of the nanocomposite membranes [52]. A decrease in the flux of PES/CZTS 2.0 wt% membrane could be explained as the agglomeration of CZTS NPs in the structure of nanocomposite membranes and clogging the pores of the smaller pore-nanocomposite membrane. Bare PES membrane supplied the lowest BSA flux (20.1 ± 3.2 L/m^2/h) (Fig. 9B). The BSA flux increased from 25.1 ± 3.5–73.8 ± 9.8 L/m^2/h when CZTS concentration increased from 0.25 to 2.00 wt.%. Furthermore, the rejection capability of the membranes towards BSA was investigated (Fig. 9C). An increase of the BSA rejection of PES/CZTS 1.0 wt% and PES/CZTS2.0 wt% membranes could be explained as both the smaller pore size and the higher hydrophilicity of the membranes compared to the PES/CZTS 0.25 wt% and PES/CZTS 0.50 wt% membranes.

3.5.2. Antifouling performance

The antifouling performance of membranes during the filtration process was also investigated by calculating of reversible fouling ratio (R_r), irreversible ratio (R_{ir}), and total fouling ratio (R_t) depending on

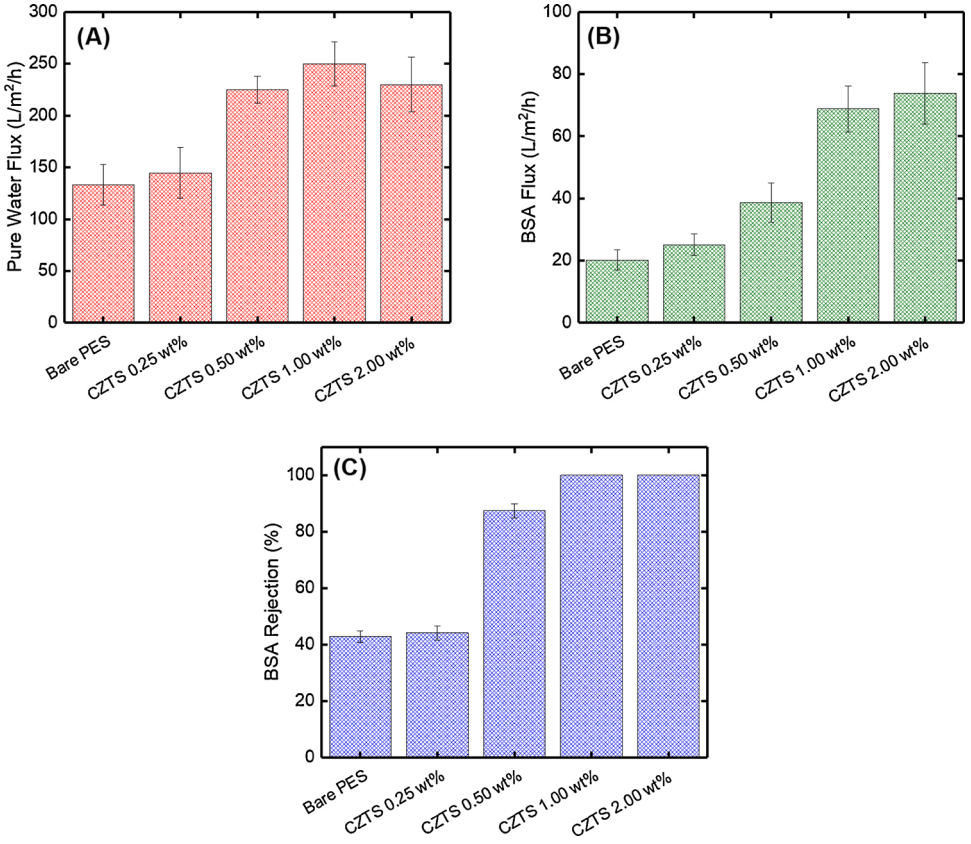

Fig. 9. The performance of CZTS NPs-blended nanocomposite membranes; **(A)** pure water flux, **(B)** BSA solution flux, and **(C)** BSA rejection.

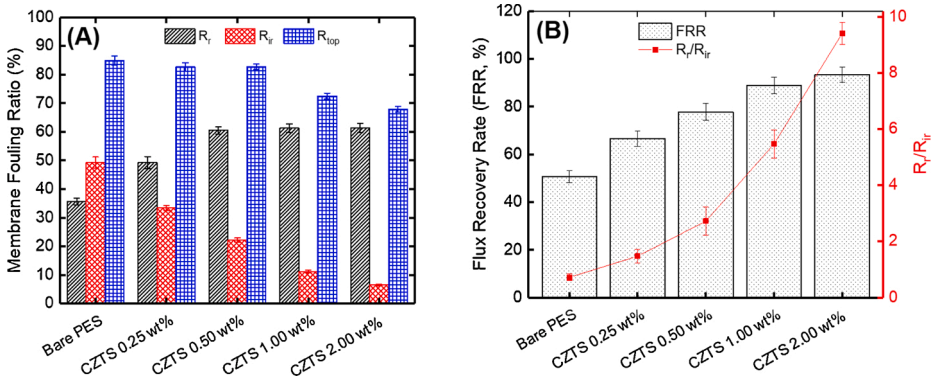

Fig. 10. **(A)** Reversible (R_r), irreversible (R_r), and total (R_t) fouling ratios of bare PES membrane and CZTS NPs-blended membranes. **(B)** Flux recovery rate (FRR) and R_r/R_{ir} ratio of bare PES membrane and CZTS NPs-blended membranes.

fluxes data. As given in Fig. 10A, R_t value of the bare PES membrane has the highest at 84.9%, indicating serious flux decline caused by BSA fouling. In comparison to bare PES membrane, the R_t values of the nanocomposite membranes (CZTS0.25, CZTS0.50, CZTS1.00, and CZTS2.00 wt.%) decrease to 82.6%, 82.8%, 72.5%, and 67.9%, respectively. Moreover, the results depicted that R_{ir} values increased while R_r values decreased after the blending of CZTS NPs (Fig. 10A). Furthermore, the flux recovery rate (FRR) and R_r/R_{ir} ratios of the membranes were shown in Fig. 10B. The increase of R_r/R_{ir} ratio approves that the irreversible membrane fouling is converted into reversible membrane fouling in the filtration process [53]. In another word, the irreversible BSA fouling in the membrane pores is inhibited due to the incorporation of CZTS NPs. R_r/R_{ir} ratio increased from 0.72 for bare PES membrane to 9.41 for CZTS 2.00 wt.% membrane. It can be explained as the formed hydration layer near the membrane surface can reduce the interaction force between the membrane surface and partially hydrophobic BSA molecules, leading to the prevention of irreversible BSA adsorption [54]. The nanocomposite membranes exhibited a higher flux recovery than the bare PES membrane. Incorporation of CZTS nanoparticles enhanced BSA fouling resistance during the filtration process and FRR values increased from 50.7% for bare PES membrane to 93.5% for CZTS 2.00 wt.% membrane. Xiang et al. [55] prepared ionic-strength-sensitive membrane via in situ cross-linked polymerization of sulfobetaine methacrylate (SBMA) in polyethersulfone (PES) solution and a liquid–liquid phase separation technique to improve anti-fouling property and blood compatibility. The results showed that the anti-fouling property and blood compatibility were considerably improved with the increase of the PSBMA content in the membrane [55].

4. Conclusions

A novel PES nanocomposite membrane incorporated with copper zinc tin sulfide nanoparticles (CZTS NPs) was prepared through the phase inversion method. First, CZTS NPs was synthesized as well as characterizated and molar ratio was optimized from 0.8 to 1.0 containing different copper and zinc ratios. The CZTS kesterite phase was evidenced through XRD patterns, outlining a unique peak at $2\theta = 28.5^\circ$ and 47.3°. CZTS1.0 sample exhibited Zn-rich composition which improved charge transfer in the heterostructure. Second, BR18 cationic azo dye removal efficiency of three heterostructures CZTS-type nanoparticles (CZTS0.8, CZTS0.9, CZTS1.0) was investigated as a photocatalyst. 88.0% degradation of BR18 dye was obtained after 3 h of irradiation under visible light radiation. No catalyst deactivation was observed after three cycles. This property was used for photo-cleaning of the nanocomposite membranes. CZTS NPs protected the surface of the nanocomposite membranes from dye contamination under visible light irridation. Third, CZTS NPs displayed effective and concentration-dependent antioxidant activity. Besides, it was determined that CZTS NPs were effective nuclease activity. The NPs exhibited their high antimicrobial activities against *Bacillus cereus*, *Pseudomonas aeruginosa*, *Legionella pneumophila* subsp. *pneumophila*. In addition to these, they indicated significant biofilm inhibition against *Staphylococcus aureus*. Results from the studies suggest that CZTS NPs can be useful material for biotechnological applications. The results also depicted that the nanocomposite membranes illustrated remarkable antifouling properties (flux recovery ratio ~94%) in contrast with the bare PES (flux recovery ratio ~51%) when BSA was filtrated as a model protein. The high retention of BSA (100%) as well as high permeation flux (73.8 ± 9.8 L/m^2/h) of the CZTS2.00 wt% membrane demonstrated that the constructed nanocomposite membrane possessed the characteristics of a promising membrane for removal of proteins from the protein-rich solution.

Funding

No funding was received for this work.

Intellectual property

We confirm that we have given due consideration to the protection of intellectual property associated with this work and that there are no impediments to publication, including the timing of publication, with respect to intellectual property. In so doing we confirm that we have followed the regulations of our institutions concerning intellectual property.

We confirm that the manuscript has been read and approved by all named authors.

We confirm that the order of authors listed in the manuscript has been approved by all named authors.

CRediT authorship contribution statement

Kasim Ocakoglu: Conceptualization, Writing - review & editing. **Nadir Dizge:** Conceptualization, Writing - original draft, Formal analysis. **Suleyman Gokhan Colak:** Investigation, Data curation. **Yasin Ozay:** Investigation, Data curation. **Zeynep Bilici:** Methodology. **M. Serkan Yalcin:** Methodology, Visualization. **Sadin Ozdemir:** Conceptualization, Writing - original draft, Formal analysis. **H. Cengiz Yatmaz:** Writing - review & editing.

Declaration of Competing Interest

The authors report no declarations of interest.

Acknowledgement

We appreciate Dr. Halil Esgin, Cukurova University Central Research Laboratory (CUMERLAB), for his help with developing all of the SEM micrographs images obtained from this research.

Appendix A. Supplementary data

Supplementary material related to this article can be found, in the online version, at doi:https://doi.org/10.1016/j.colsurfa.2021.126230.

References

[1] J.N. Edokpayi, J.O. Odiyo, O.S. Durowoju, Impact of Wastewater on Surface Water Quality in Developing Countries: A Case Study of South Africa, Water Qual., InTech, 2017, https://doi.org/10.5772/66561.
[2] M.B. Ahmed, J.L. Zhou, H.H. Ngo, W. Guo, N.S. Thomaidis, J. Xu, Progress in the biological and chemical treatment technologies for emerging contaminant removal from wastewater: a critical review, J. Hazard. Mater. 323 (2017) 274–298, https://doi.org/10.1016/j.jhazmat.2016.04.045.
[3] S. Shirazi, C.-J. Lin, D. Chen, Inorganic fouling of pressure-driven membrane processes — a critical review, Desalination. 250 (2010) 236–248, https://doi.org/10.1016/j.desal.2009.02.056.
[4] S. Hube, M. Eskafi, K.F. Hrafnkelsdóttir, B. Bjarnadóttir, M.Á. Bjarnadóttir, S. Axelsdóttir, B. Wu, Direct membrane filtration for wastewater treatment and resource recovery: a review, Sci. Total Environ. 710 (2020) 136375, https://doi.org/10.1016/j.scitotenv.2019.136375.
[5] B. Van Der Bruggen, C. Vandecasteele, T. Van Gestel, W. Doyen, R. Leysen, A review of pressure-driven membrane processes in wastewater treatment and drinking water production, Environ. Prog. Sustain. Energy 22 (2003) 46–56, https://doi.org/10.1002/ep.670220116.
[6] B. Van der Bruggen, L. Lejon, C. Vandecasteele, Reuse, Treatment, and Discharge of the Concentrate of Pressure-Driven Membrane Processes, Environ. Sci. Technol. 37 (2003) 3733–3738, https://doi.org/10.1021/es0201754.
[7] X. Qu, P.J.J. Alvarez, Q. Li, Applications of nanotechnology in water and wastewater treatment, Water Res. 47 (2013) 3931–3946, https://doi.org/10.1016/j.watres.2012.09.058.
[8] K.M.M. Abou El-Nour, A. Eftaiha, A. Al-Warthan, R.A.A. Ammar, Synthesis and applications of silver nanoparticles, Arab. J. Chem. 3 (2010) 135–140, https://doi.org/10.1016/j.arabjc.2010.04.008.
[9] I. Khan, K. Saeed, I. Khan, Nanoparticles: properties, applications and toxicities, Arab. J. Chem. 12 (2019) 908–931, https://doi.org/10.1016/j.arabjc.2017.05.011.
[10] D. Guo, G. Xie, J. Luo, Mechanical properties of nanoparticles: basics and applications, J. Phys. D Appl. Phys. 47 (2014) 013001, https://doi.org/10.1088/0022-3727/47/1/013001.
[11] J. Gao, H. Gu, B. Xu, Multifunctional magnetic nanoparticles: design, synthesis, and biomedical applications, Acc. Chem. Res. 42 (2009) 1097–1107, https://doi.org/10.1021/ar9000026.
[12] A. Ito, M. Shinkai, H. Honda, T. Kobayashi, Medical application of functionalized magnetic nanoparticles, J. Biosci. Bioeng. 100 (2005) 1–11, https://doi.org/10.1263/jbb.100.1.
[13] S. Prabhu, E.K. Poulose, Silver nanoparticles: mechanism of antimicrobial action, synthesis, medical applications, and toxicity effects, Int. Nano Lett. (2012), https://doi.org/10.1186/2228-5326-2-32.
[14] T. Xiang, J. Hou, H. Xie, X. Liu, T. Gong, S. Zhou, Biomimetic micro/nano structures for biomedical applications, Nano Today 35 (2020) 100980, https://doi.org/10.1016/j.nantod.2020.100980.
[15] L.Y. Ng, A.W. Mohammad, C.P. Leo, N. Hilal, Polymeric membranes incorporated with metal/metal oxide nanoparticles: a comprehensive review, Desalination 308 (2013) 15–33, https://doi.org/10.1016/j.desal.2010.11.033.
[16] M. Wang, L. Wu, C. Gao, The influence of phase inversion process modified by chemical reaction on membrane properties and morphology, J. Memb. Sci. 270 (2006) 154–161, https://doi.org/10.1016/j.memsci.2005.06.051.
[17] G. Wu, S. Gan, L. Cui, Y. Xu, Preparation and characterization of PES/TiO 2 composite membranes, Appl. Surf. Sci. (2008), https://doi.org/10.1016/j.apsusc.2008.05.221.
[18] V. Vatanpour, S.S. Madaeni, L. Rajabi, S. Zinadini, A.A. Derakhshan, Boehmite nanoparticles as a new nanofiller for preparation of antifouling mixed matrix membranes, J. Memb. Sci. 401–402 (2012) 132–143, https://doi.org/10.1016/j.memsci.2012.01.040.
[19] N. Maximous, G. Nakhla, W. Wan, K. Wong, Preparation, characterization and performance of Al2O3/PES membrane for wastewater filtration, J. Memb. Sci. 341 (2009) 67–75, https://doi.org/10.1016/j.memsci.2009.05.040.
[20] J. Shen, H. Ruan, L. Wu, C. Gao, Preparation and characterization of PES–SiO2 organic–inorganic composite ultrafiltration membrane for raw water pretreatment, Chem. Eng. J. 168 (2011) 1272–1278, https://doi.org/10.1016/j.cej.2011.02.039.
[21] A.G. Kannan, T.E. Manjulavalli, J. Chandrasekaran, Influence of solvent on the properties of CZTS nanoparticles, Procedia Eng. 141 (2016) 15–22, https://doi.org/10.1016/j.proeng.2015.08.1112.
[22] M. Sridharan, P. Kamaraj, Y.S. Huh, S. Devikala, M. Arthanareeswari, J.A. Selvi, E. Sundaravadivel, Quaternary CZTS nanoparticle decorated CeO 2 as a noble metal free p–n heterojunction photocatalyst for efficient hydrogen evolution, Catal. Sci. Technol. 9 (2019) 3686–3696, https://doi.org/10.1039/C9CY00429G.
[23] Z. Bilici, Z. Işık, Y. Aktaş, H.C. Yatmaz, N. Dizge, Photocatalytic effect of zinc oxide and magnetite entrapped calcium alginate beads for azo dye and hexavalent chromium removal from solutions, J. Water Process Eng. 31 (2019) 100826, https://doi.org/10.1016/j.jwpe.2019.100826.
[24] M.S. BLOIS, Antioxidant determinations by the use of a stable free radical, Nature 181 (1958) 1199–1200, https://doi.org/10.1038/1811199a0.
[25] T.C.P. Dinis, V.M.C. Madeira, L.M. Almeida, Action of phenolic derivatives (Acetaminophen, salicylate, and 5-Aminosalicylate) as inhibitors of membrane lipid peroxidation and as peroxyl radical scavengers, Arch. Biochem. Biophys. 315 (1994) 161–169, https://doi.org/10.1006/abbi.1994.1485.
[26] G.A. Martínez-Castañón, N. Niño-Martínez, F. Martínez-Gutierrez, J.R. Martínez-Mendoza, F. Ruiz, Synthesis and antibacterial activity of silver nanoparticles with different sizes, J. Nanopart. Res. 10 (2008) 1343–1348, https://doi.org/10.1007/s11051-008-9428-6.
[27] Lowry, Lowry protein assay, J. Biol. Chem. (1951).
[28] H. Barzegar, M.A. Zahed, V. Vatanpour, Antibacterial and antifouling properties of Ag3PO4/GO nanocomposite blended polyethersulfone membrane applied in dye separation, J. Water Process Eng. 38 (2020) 101638, https://doi.org/10.1016/j.jwpe.2020.101638.
[29] H. Katagiri, K. Jimbo, M. Tahara, H. Araki, K. Oishi, The influence of the compositionratio on CZTS-based thinfilmsolarcells, in: MRS Proc., 1165, 2009, https://doi.org/10.1557/PROC-1165-M04-01, 1165-M04-01.
[30] L. Korala, M.B. Braun, J.M. Kephart, Z. Tregillus, A.L. Prieto, Ligand-Exchanged CZTS Nanocrystal Thin Films: Does Nanocrystal Surface Passivation Effectively Improve Photovoltaic Performance? Chem. Mater. 29 (2017) 6621–6629, https://doi.org/10.1021/acs.chemmater.7b00541.
[31] S.A. Phaltane, S.A. Vanalakar, T.S. Bhat, P.S. Patil, S.D. Sartale, L.D. Kadam, Photocatalytic degradation of methylene blue by hydrothermally synthesized CZTS nanoparticles, J. Mater. Sci. Mater. Electron. 28 (2017) 8186–8191, https://doi.org/10.1007/s10854-017-6527-0.
[32] A. Méndez-López, A. Morales-Acevedo, Y.J. Acosta-Silva, M. Ortega-López, Synthesis and characterization of colloidal CZTS nanocrystals by a hot-injection method, . (2016), https://doi.org/10.1155/2016/7486094.
[33] Y.M. Hunge, Basics and advanced developments in photocatalysis – a review (Mini review), Int. J. Hydrol. 2 (2018), https://doi.org/10.15406/ijh.2018.02.00122.
[34] Y.M. Hunge, V.S. Mohite, S.S. Kumbhar, K.Y. Rajpure, A.V. Moholkar, C. H. Bhosale, Photoelectrocatalytic degradation of methyl red using sprayed WO3 thin films under visible light irradiation, J. Mater. Sci. Mater. Electron. 26 (2015) 8404–8412, https://doi.org/10.1007/s10854-015-3508-z.
[35] N.M. Mahmoodi, A. Maghsoodi, Kinetics and isotherm of cationic dye removal from multicomponent system using the synthesized silica nanoparticle, Desalin. Water Treat. 54 (2015) 562–571, https://doi.org/10.1080/19443994.2014.880158.
[36] N.M. Mahmoodi, Magnetic ferrite nanoparticle–alginate composite: synthesis, characterization and binary system dye removal, J. Taiwan Inst. Chem. Eng. 44 (2013) 322–330, https://doi.org/10.1016/j.jtice.2012.11.014.
[37] F. Duman, I. Ocsoy, F.O. Kup, Chamomile flower extract-directed CuO nanoparticle formation for its antioxidant and DNA cleavage properties, Mater. Sci. Eng. C. 60 (2016) 333–338, https://doi.org/10.1016/j.msec.2015.11.052.
[38] R. Merugu, R. Gothalwal, P. Kaushik Deshpande, S. De Mandal, G. Padala, K. Latha Chitturi, Synthesis of Ag/Cu and Cu/Zn bimetallic nanoparticles using toddy palm: investigations of their antitumor, antioxidant and antibacterial activities, Mater. Today Proc. (2020), https://doi.org/10.1016/j.matpr.2020.08.027.
[39] C.H. Foyer, G. Noctor, Redox homeostasis and antioxidant signaling: a metabolic interface between stress perception and physiological responses, Plant Cell (2005), https://doi.org/10.1105/tpc.105.033589.
[40] D.M. Grochowski, S. Uysal, A. Aktumsek, S. Granica, G. Zengin, R. Ceylan, M. Locatelli, M. Tomczyk, In vitro enzyme inhibitory properties, antioxidant activities, and phytochemical profile of Potentilla thuringiaca, Phytochem. Lett. 20 (2017) 365–372, https://doi.org/10.1016/j.phytol.2017.03.005.
[41] Z. Wei, L. Wang, C. Tang, S. Chen, Z. Wang, Y. Wang, J. Bao, Y. Xie, W. Zhao, B. Su, C. Zhao, Metal-Phenolic Networks Nanoplatform to Mimic Antioxidant Defense System for Broad-Spectrum Radical Eliminating and Endotoxemia Treatment, Adv. Funct. Mater. 30 (2020) 2002234, https://doi.org/10.1002/adfm.202002234.
[42] A.A. Bazrafshan, M. Ghaedi, S. Hajati, R. Naghiha, A. Asfaram, Synthesis of ZnO-nanorod-based materials for antibacterial, antifungal activities, DNA cleavage and efficient ultrasound-assisted dyes adsorption, Ecotoxicol. Environ. Saf. 142 (2017) 330–337, https://doi.org/10.1016/j.ecoenv.2017.04.011.
[43] U.V. Kamble, S.A. Patil, P.S. Badami, DNA cleavage and antimicrobial studies of 17-membered schiff base macrocyclic triazoles: synthesis and spectroscopic approach, J. Incl. Phenom. Macrocycl. Chem. 68 (2010) 347–358, https://doi.org/10.1007/s10847-010-9794-4.
[44] M. Carbone, R. Briancesco, L. Bonadonna, Antimicrobial power of Cu/Zn mixed oxide nanoparticles to Escherichia coli, Environ. Nanotechnol. Monit. Manag. 7 (2017) 97–102, https://doi.org/10.1016/j.enmm.2017.01.005.
[45] S. Saedi, M. Shokri, J.-W. Rhim, Antimicrobial activity of sulfur nanoparticles: Effect of preparation methods, Arab. J. Chem. 13 (2020) 6580–6588, https://doi.org/10.1016/j.arabjc.2020.06.014.
[46] A. Valliammai, S. Sethupathy, A. Priya, A. Selvaraj, J.P. Bhaskar, V. Krishnan, S. K. Pandian, 5-Dodecanolide interferes with biofilm formation and reduces the virulence of Methicillin-resistant Staphylococcus aureus (MRSA) through up regulation of agr system, Sci. Rep. 9 (2019) 13744, https://doi.org/10.1038/s41598-019-50207-y.

[47] N.A. Jasim, F.A. Al-Gasha'a, M.F. Al-Marjani, A.H. Al-Rahal, H.A. Abid, N.A. Al-Kadhmi, M. Jakaria, A.M. Rheima, ZnO nanoparticles inhibit growth and biofilm formation of vancomycin-resistant S. Aureus (VRSA), Biocatal. Agric. Biotechnol. 29 (2020) 101745, https://doi.org/10.1016/j.bcab.2020.101745.
[48] A. Akbar, M.B. Sadiq, I. Ali, N. Muhammad, Z. Rehman, M.N. Khan, J. Muhammad, S.A. Khan, F.U. Rehman, A.K. Anal, Synthesis and antimicrobial activity of zinc oxide nanoparticles against foodborne pathogens Salmonella typhimurium and Staphylococcus aureus, Biocatal. Agric. Biotechnol. 17 (2019) 36–42, https://doi.org/10.1016/j.bcab.2018.11.005.
[49] L. Miao, P. Wang, J. Hou, D. Ning, Z. Liu, S. Liu, T. Li, Chronic exposure to CuO nanoparticles induced community structure shift and a delay inhibition of microbial functions in multi-species biofilms, J. Clean. Prod. 262 (2020) 121353, https://doi.org/10.1016/j.jclepro.2020.121353.
[50] G. Applerot, J. Lellouche, N. Perkas, Y. Nitzan, A. Gedanken, E. Banin, ZnO nanoparticle-coated surfaces inhibit bacterial biofilm formation and increase antibiotic susceptibility, RSC Adv. 2 (2012) 2314, https://doi.org/10.1039/c2ra00602b.
[51] S. Dwivedi, R. Wahab, F. Khan, Y.K. Mishra, J. Musarrat, A.A. Al-Khedhairy, Reactive oxygen species mediated bacterial biofilm inhibition via zinc oxide nanoparticles and their statistical determination, PLoS One 9 (2014) e111289, https://doi.org/10.1371/journal.pone.0111289.
[52] M.S. Sri Abirami Saraswathi, A. Nagendran, D. Rana, Tailored polymer nanocomposite membranes based on carbon, metal oxide and silicon nanomaterials: a review, J. Mater. Chem. A 7 (2019) 8723–8745, https://doi.org/10.1039/C8TA11460A.
[53] X. Shen, T. Xie, J. Wang, P. Liu, F. Wang, An anti-fouling poly(vinylidene fluoride) hybrid membrane blended with functionalized ZrO 2 nanoparticles for efficient oil/water separation, RSC Adv. 7 (2017) 5262–5271, https://doi.org/10.1039/C6RA26651G.
[54] B.A. Russell, K. Kubiak-Ossowska, P.A. Mulheran, D.J.S. Birch, Y. Chen, Locating the nucleation sites for protein encapsulated gold nanoclusters: a molecular dynamics and fluorescence study, Phys. Chem. Chem. Phys. 17 (2015) 21935–21941, https://doi.org/10.1039/C5CP02380G.
[55] T. Xiang, C.D. Luo, R. Wang, Z.Y. Han, S.D. Sun, C.S. Zhao, Ionic-strength-sensitive polyethersulfone membrane with improved anti-fouling property modified by zwitterionic polymer via in situ cross-linked polymerization, J. Memb. Sci. (2015), https://doi.org/10.1016/j.memsci.2014.11.045.